International Journal of Pharmaceutics 688 (2026) 126441

Contents lists available at ScienceDirect

International Journal of Pharmaceutics

journal homepage: www.elsevier.com/locate/ijpharm

Investigation of structural and thermal properties of solid lipid-based nanocarriers optimized by microfluidic synthesis

Giulia Gabbricci [a,b,c,1], Luigi Talarico [a,b,c,1], Ilaria Clemente [a,b,c,*], Aleksi Sutinen [d], Clément E. Blanchet [d], Duccio Tatini [a,b], Gemma Leone [a,b,c], Agnese Magnani [a,b,c,**]

[a] Department of Biotechnology, Chemistry and Pharmacy, University of Siena, Via Aldo Moro 2, 53100 Siena, Italy
[b] CSGI - Consorzio Interuniversitario Sistemi Grande Interfase - Siena Research Group, Via della Lastruccia 3, Sesto Fiorentino, Italy
[c] INSTM - Consorzio Interuniversitario Nazionale per la Scienza e Tecnologia dei Materiali - Siena Research Unit, Via G. Giusti 9, Firenze, Italy
[d] European Molecular Biology Laboratory (EMBL), Hamburg Outstation c/o DESY, Notkestrasse 85, 22607 Hamburg, Germany

ARTICLE INFO

Keywords:
Solid lipid nanoparticles
Nanostructured lipid carriers
Microfluidics
Design of experiments
Time resolved-SAXS
Assembly kinetics

ABSTRACT

In the past decade, lipid-based nanocarriers have gained increasing popularity as the emergent technology for drug delivery, owing to the capability to protect the bioactive cargo and improve intracellular transport and release. Since their approval for clinical usage several lipid nanocarrier formulations were investigated to obtain optimal physicochemical properties and enhanced therapeutic efficacy. Among the factors influencing structure, stability and cellular uptake, the choice of lipid components plays a major role. Moreover, surfactant coatings mediate interactions with membranes and provide stealth and permeation properties. Thus, manipulation of composition and relative abundance results in dramatic modification of physicochemical properties and functionality. Microfluidic-assisted preparation of lipid nanocarriers allows to obtain stable formulations with high reproducibility, boosting screening and optimization potential. However, the fundamental understanding of the mechanism and kinetics of assembly of these systems is still lacking. This knowledge is crucial since early-stage aggregation and transient structures of non-equilibrium systems influence their stability, storage and shelf life, thus impacting greatly on formulation efficacy. In this work, high-throughput screening and optimization of two types of nanocarriers based on solid lipids, i.e. SLNs and NLCs are proposed. Microfluidic synthesis allowed the screening of lipid/surfactant components and instrumental settings following an experimental design approach. By this method, robust models were obtained to describe the influence of each parameter on the final nanocarrier properties. Supramolecular and thermal characterization by means of Dynamic Light Scattering, synchrotron static and Time-Resolved Small Angle X-ray Scattering, Differential Scanning Calorimetry, and quantification of encapsulation efficiency of two model drugs by High Performance Liquid Chromatography gave significant insights for rational design of lipid-based nanoparticles. The fundamental understanding of the mechanism and kinetics of assembly of these systems allowed to correlate structural and dynamic properties to carrier functionality and stability.

1. Introduction

Lipid-based nanocarrier formulations represent the emergent technology in drug delivery science in the last three decades that has witnessed a remarkable growth. The large applicative potential of these systems and their recent clinical success as the delivery platform for nucleic acid-based vaccines (i.e. Covid-19 Moderna and Pfizer formulations), resulted in novel nanovector technologies advancing conventional transport and release systems (Sebastiani et al., 2021; Samaridou et al., 2020). Among several novel types of lipid carriers, Solid Lipid Nanoparticles (SLNs) and Nanostructured Lipid Carriers (NLCs) represent some of the recent advances in terms of formulation stability,

* Corresponding author at: Department of Biotechnology, Chemistry and Pharmacy, University of Siena, Via Aldo Moro 2, 53100 Siena, IT, Italy.
** Corresponding author at: CSGI - Consorzio Interuniversitario Sistemi Grande Interfase - Siena Research Group, Via della Lastruccia 3, Sesto Fiorentino, IT, Italy.
E-mail addresses: ilaria.clemente2@unisi.it (I. Clemente), agnese.magnani@unisi.it (A. Magnani).
[1] co-first authors.

https://doi.org/10.1016/j.ijpharm.2025.126441
Received 13 September 2025; Received in revised form 13 November 2025; Accepted 27 November 2025
Available online 4 December 2025

enhanced encapsulation and protection, and efficient targeting and delivery (Tenchov et al., 2021; Müller et al., 2002).

Solid Lipid Nanoparticles possess a solid lipidic core that favors encapsulation and protection of the bioactive cargo, particularly lipophilic drugs from degradation and leaking due to the presence of an internal liquid crystalline arrangement, stabilized by a surfactant shell. The polymorphism of most used solid lipids enables the entrapment of drugs in the defects of the metastable quasi-ordered lipid lattice (α-form) and their release over time following transitions to a more ordered, thermodynamically stable configuration (β-form) (Campani et al., 2018; Koroleva et al., 2022; Sakellari et al., 2021). Even though the SLNs core is solid at ambient temperature and commonly used solid lipids are completely melted around 60 °C, the phase transition starts at considerably lower temperatures, comparable with physiologically relevant ones (above 32–33 °C). This property grants core stability in storage conditions and drug release upon administration. The nature of the solid lipid determines the melting and transition temperatures from one polymorphic state to the other, by modifying the core structure and thus influencing cargo release and dispersion stability. The presence of a surfactant coating grants enhanced stability of the core, preventing interparticle aggregation over time. However, several aspects governing these processes are still largely uncertain. Particularly, it is known that the polymorphic transitions of the lipid core affect dispersion stability and accelerate degradation of the cargo, and that shell-core interactions influence surface structure and location of entrapped drugs (Campani et al., 2018; Koroleva et al., 2022). Nanostructured Lipid Carriers represent a technological advancement of SLNs, developed to improve issues related to stability of the internal structure, leaking of drug due to phase transitions, and interparticle aggregation. This is done through modification of the nanoparticle core by substituting a fraction of the solid lipid with a liquid lipid in varying ratios. This combination of amorphous and quasi-ordered domains in the core organization should grant improved stability and cargo retention (Sakellari et al., 2021; Khater et al., 2021). Thus, rational choice of lipid/surfactant composition and relative abundance can result in enhanced control on structural and functional properties.

Particularly, several manipulations have been attempted to obtain specific physicochemical properties (Spinozzi et al., 2024) that directly impact on the final formulation. Up to date the investigation in this promising field followed a trial-and-error approach that allowed scientists to obtain nanocarriers with huge clinical potential, however comprehensive investigation of their properties has been often overlooked. (Wang et al., 2019). This vast production facilitated the formulation of effective nanocarriers, at the expense of the investigation of the parameters influencing structure, assembly process, size and surface properties (Chang et al., 2012). These factors critically impact on the effectiveness and applicability of the formulation. Thus, it appears that rational design and optimization of composition and synthetic parameters for each specific formulation is key.

One of the limitations in screening capability of lipid-based formulations is the wide set of lipids, surfactants and synthetic conditions to be tested. Microfluidic-assisted synthetic processes have granted the possibility to perform high-throughput synthesis with elevated precision and reproducibility, thus minimizing the operator-dependent variability (Chen et al., 2012; Arduino et al., 2021). This apparatus generally includes a system of pumps and micro tubings where two fluids, i.e. the aqueous and organic phases respectively, are injected in the chip at microliter-controlled flow rates. Here, a pattern of microchannels engraved with a specific geometry allows the mixing and nanocarrier assembly.. This allows the screening of several experimental parameters with minimal time and reagent consumption by precisely controlling the synthetic conditions. The most relevant are the total flow rates of the phases, the fractionated flow rate (FFR) that indicates their respective mixing ratios, and the chip geometry that determines interfacial fluid mixing (Maeki et al., 2022). Nevertheless, one important limitation lies in the gap of knowledge about the correlation between the chosen instrumental parameters and the resulting aggregation kinetics, structural stability and encapsulation efficiency of the obtained nanosystems (Gimondi et al., 2023).

As a matter of fact, the actual low availability of pharmaceuticals and personal care products based on nanoparticulate systems is mainly due to the difficulty in controlling batch-to-batch quality and reproducibility. Indeed, the final physicochemical properties of these systems are very susceptible to changes in their production processes, and current regulations require high standards in the uniformity of samples dimension and monodispersity (Pepic et al., 2014, 1005.). In this context, the application of principles of Design of Experiments (DoE) and Quality by design (QbD) (Talarico et al., 2023), that are funded on a comprehensive understanding of the synthetical process and its influence on the final product, can lead to a final optimized synthetical routine. This approach can give insights into the influence of different independent parameters and their statistical correlation to the final system properties. Thus, the application of DoE is fundamental from early-stage research to simplify the experimental routines through rationalization of the trial-and-error approach, and obtain a robust procedure with minimal amount of synthetical runs (González-Fernández et al., 2021; Shah et al., 2015; Tavares Luiz and Viegas, 2021).

In this work, we investigate microfluidic-synthetized SLNs and NLCs as carriers of two model drugs, i.e. resveratrol and hydroquinone, through synthesis optimization by Design of Experiments and advanced physico-chemical characterization. Through this approach we aim to integrate robust statistics in the design of nanocarrier candidates, and in-depth investigation of the structure, kinetics and stability, that directly impact the nanocarrier functionality. The two molecules were chosen as representative models for hydrophobic and hydrophilic cargoes respectively, with different affinity to the carrier. The two proposed nanocarrier series were synthesized by using a commercial microfluidic apparatus, and the influence of both compositional and instrumental parameters on the final properties was modeled. Size, PDI and encapsulation efficiency determined by Dynamic Light Scattering (DLS) and High-Performance Liquid Chromatography (HPLC) were the selected responses to explore the design space. Indeed, they represent the preliminary physicochemical properties to evaluate for an optimal final formulation. Moreover, these measurements are fast and reliable, thus appropriate for a high-throughput screening of large sample sets. This allowed to select the parameters to obtain the final optimized nanosystems, that were further investigated by Differential Scanning Calorimetry (DSC), laboratory Small Angle X-ray Scattering, synchrotron static and Time-resolved Small Angle X-ray Scattering (Tr-SAXS).The systematic approach to synthesis optimization combined with fast and reliable microfluidic synthesis allows significant advances in lipid-based nanoparticle research and production. To our knowledge, there are currently no other reported works where SLNs and NLCs have been optimized by combining microfluidics and DoE, and then their fundamental properties investigated by advanced combined techniques. The integration of these approaches enables an enhanced control over synthetic conditions, scalability and translation capability of the systems, as statistically validated instrumental parameters are directly transferable from lab-scale experiments to industrial production.

2. Materials and methods

2.1. Materials

Precirol ATO 5 – a commercial lipid mixture composed mainly of esters of palmitic (16:0) and stearic (18:0) fatty acids, with the diester fraction being predominant – was kindly provided by Gattefossè (Saint-Priest, France). Oleic acid (99 %), Poloxamer 407 (triblock copolymer made from a central polypropylene glycol and two polyethylene glycol blocks, reagent grade), Resveratrol (3,4′,5-*trans*-trihydroxystilbene, analytical standard, 99 %), Hydroquinone (benzene 1–4 diol, ReagentPlus®, 99 %), Ethanol (absolute), Methanol (gradient grade), and formic

acid (98–100 % for HPLC LiChropur™) were purchased from Sigma Aldrich (Milano, Italy). Phree SPE cartridges were purchased from Phenomenex (Torrance, CA, USA).

2.2. Microfluidic synthesis of SLNs and NLCs

For SLNs production a microfluidic apparatus Automated Nanoparticle System (ANP, Particle Works, Unchained Labs, UK) was used with a 190 μm Junction chip (Dolomite, Unchained Labs, UK). An aqueous phase containing the surfactant (Poloxamer 407) and an organic phase (ethanol) containing the solid lipid (Precirol ATO 5) and the active molecule (Resveratrol or Hydroquinone) were injected into the apparatus. The chip was immersed in a water bath at 70 °C to maintain the lipid melted during the synthesis. The total flow rate (TFR) was 8 mL/min, and the flow fractionated ratio (FFR) i.e. the aqueous-to-organic phase ratio was variable according to the experimental design runs (Table 1, factor C). For NLCs production the same method was followed, and a fraction of the total lipid content was substituted with the liquid lipid (Oleic Acid) into the organic phase (Table 2, factor D). Each synthesis was performed with a volume head and tail cut each corresponding to 10 % of the collected volume. The obtained dispersions were then cooled in an ice bath for 15 min to induce rapid and homogeneous core solidification and structuring (Sebastiani et al., 2021; Duong et al., 2020).

2.3. Dynamic Light Scattering (DLS)

Particle size distribution i.e. hydrodynamic diameter and polydispersity index (PDI) were determined using a Zetasizer Ultra RED system (Malvern, UK) with a backscatter (173°) detector angle. All samples were measured in triplicate with the mean size and standard deviation (SD) of the replicates reported. Analysis of results was performed by ZS Explorer software by Malvern Panalytical, that employs Cumulants analysis.

DLS scans in temperature were performed on empty SLNs and NLCs to investigate potential temperature-dependent changes in the size and PDI. Measurements were performed at 25 °C, 40 °C, 50 °C, 60 °C, 70 °C, and then cooling back at 25 °C with an equilibration time of 5 min.

2.4. Experimental factorial design

In this work, four independent two-level full factorial designs were implemented to model the linear influence of different synthetical parameters (or "factors", Tables 1 and 2) on the size, PDI and encapsulation efficiency (or "responses", Tables 1 and 2) of SLNs and NLCs loaded either with Resveratrol or Hydroquinone (acronyms in Table 3). For either Resveratrol or Hydroquinone loaded SLNs, the influence of the lipid (Precirol ATO 5) concentration, the surfactant (Poloxamer 407) concentration and the aqueous/organic flow rate (FFR) during the synthesis was evaluated with a 2-level, 3-factors full factorial design. Each run was performed in quadruplicate for better statistics. This resulted in 16 suggested syntheses (or "runs") to explore the design space and investigate the optimal value for each factor (Tables S1 and S3). For either Resveratrol or Hydroquinone loaded NLCs, two independent 2-levels, 4-factors full factorial designs were conducted using the same factors studied for SLNs, with the addition of the weight percentage of liquid lipid (Oleic Acid) with respect to the solid lipid. Each run was performed in quadruplicate for better statistics. This resulted in 32 suggested syntheses (or "runs") to explore the design space and investigate the optimal value for each factor (Tables S2 and S4). The factors and their levels were chosen based on pre-formulation studies and are reported with the monitored dependent variable in Tables 1 and 2. The loaded quantity of either encapsulated compound was kept constant at 0.5 mg/mL. For each suggested run the responses were measured by DLS and HPLC and then modeled.

To identify the significance of the selected independent factors and their linear interactions, analysis of variance (ANOVA) was performed for each experimental response. A p-value less than 0.05 was considered statistically significant to the models. Design Expert 13.0.5.0 software was used for DoE and statistics.

For each experimental design, an optimized formulation was obtained by using a desirability function with the aim of maximizing the encapsulation efficiency and minimizing the size and the PDI (i.e. by assigning a major relative importance to increasing the encapsulation efficiency). The optimal formulation for each system was synthesized to validate the predictive model, and then used for further physicochemical characterizations.

Table 1
2^3 full factorial design for either Resveratrol or Hydroquinone loaded SLNs, where the independent variables are the synthetic parameters, the levels are the tested values for each parameter and the dependent variables are the experimentally measured responses.

Independent variables (or factors)	Coded levels		Dependent variables (or responses)
	−1	+1	
A: Solid Lipid concentration (mg/mL)	1.5	2.5	Size (nm)
B: Surfactant concentration (mg/mL)	1	2.5	PDI
C: FFR	2	3	Encapsulation Efficiency (%)

Table 2
2^4 full factorial design for either Resveratrol or Hydroquinone loaded NLCs, where the independent variables are the synthetic parameters, the levels are the tested values for each parameter and the dependent variables are the experimentally measured responses.

Independent variables	Coded levels		Dependent variables
	−1	+1	
A: Solid Lipid concentration (mg/mL)	1.5	2.5	Size (nm)
B: Surfactant concentration (mg/mL)	1	2.5	PDI
C: FFR	2	3	Encapsulation Efficiency (%)
D: Liquid Lipid (%w/w)	25	50	

Table 3
Acronyms for each sample, and minimum and maximum values of the three chosen responses i.e. size, PDI and EE through the studied design spaces.

Sample name	Size (nm)	PDI	Encapsulation efficiency (%)
Resv-SLN	57.8–263.5	0.09–0.5	20.6–49.3
Resv-NLC	41.1–106.4	0.17–0.53	6.6–42.8
Hq-SLN	52.5–665.8	0.1–0.4	3.6–14.5
Hq-NLC	50.3–290.5	0.18–0.51	2.0–15.0

2.5. Purification of lipid nanoparticles

The obtained nanoparticle formulations were dialyzed against at least 200 volumes of MilliQ water using a dialysis kit (Pur-A-lyzerTM Midi Dialysis Kit, Sigma, UK) to remove the unencapsulated cargo. The post-dialysis solution of nanoparticles was stored at 4 °C for further investigation.

2.6. HPLC-DAD for encapsulation efficiency

The encapsulation efficiency was determined using a direct method. Briefly, 0.1 mL of the purified samples were diluted with 0.9 mL of methanol and vortexed at 8000 rpm for 2 min to destroy the

nanoparticles and free the encapsulated cargo. Subsequently, the sample was eluted by using a positive pressure manifold in a solid phase extraction Phree™ SPE cartridge (Phenomenex, Torrance, CA, USA) to selectively remove lipids from the solution. SPE cartridges were previously conditioned by eluting 1 mL of methanol. This purified sample, containing only the previously encapsulated cargo, was then analyzed by HPLC-DAD (Thermo Fisher UltiMate 3000, Monza, Italy) as follows.

For Resveratrol quantification a Kinetex C18 Polar column (250 × 2.1 mm, 100 Å, 2.6 µm, Phenomenex, Torrance, CA, USA) was used following an isocratic method with 30:60 (% v/v) H_2O and Methanol both acidified with 0.1 % (v/v) formic acid. The flow rate was set at 0.4 mL/min, and the column temperature was kept at 40 °C. All the chromatograms were recorded at 306 nm. Samples were quantified by interpolation with a linear calibration curve obtained from 1 to 30 ppm (mg/L).

For Hydroquinone quantification a Kinetex Biphenyl column (250 × 2.1 mm, 100 Å, 2.6 µm, Phenomenex, Torrance, CA, USA) was used. An isocratic method was used, with 70:30 (%v/v) of H_2O and Methanol both acidified with 0.1 % (v/v) formic acid. The flow rate was 0.4 mL/min and the column temperature was kept at 35 °C. All the chromatograms were recorded at 274 nm. Samples were quantified by interpolation with a linear calibration curve obtained between 1 to 50 ppm (mg/L). The obtained amount of encapsulated cargo was used to determine the EE(%) as follows (Eq. (1)), where m_{loaded} corresponds to the amount of encapsulated cargo and m_{total} the amount used during each experimental run. Representative chromatograms are reported in figure S15.

$$EE(\%) = \frac{m_{loaded}}{m_{total}} \times 100 \tag{1}$$

Limit of Detection (LOD) and Limit of Quantification (LOQ) were obtained as described by International Committee of Harmonization (ICH) and European Medicine Agencies (EMA) guidelines. Specifically, the amount of encapsulated cargo was obtained after peak integration and interpolation with a calibration curve both for Resveratrol (R2 = 0.997, LOD = 0.08 ppm, LOQ = 0.26 ppm) and Hydroquinone (R2 = 0.999, LOD = 0.05 ppm, LOQ = 0.16 ppm).

2.7. Differential Scanning Calorimetry

Aliquots of 10 µL of each optimized loaded and unloaded SLNs and NLCs dispersions were placed in a hermetic stainless-steel pan for differential scanning calorimetry (DSC) experiments. The thermal behavior of the dispersion was characterized on a DSC Q2500 (TA instruments) with the following temperature program: isothermal for 5 min at 10 °C, a 2 °C/min temperature ramp between 10 and 70 °C. The same experimental procedure was applied to the bulk lipid. An empty aluminum pan was used as a reference. Enthalpy, onset and peak temperatures were acquired through Trios Software. The crystallinity (χ%) of each nanodispersion was calculated in relation to the bulk lipid material constituting both SLNs and NLCs using Eq. (2):

$$\chi\% = \frac{\Delta H_{sample}}{\Delta H_{bulklipid} \times lipidconcentration} \times 100 \tag{2}$$

where ΔH stands for both the areas under the curve for the main endothermic events in the sample and in the bulk lipid respectively. Crystallinity data were normalized for the lipid concentration in the sample.

2.8. Laboratory Small Angle X-ray Scattering measurements

Firstly, unloaded SLNs and NLCs were measured by static Small and Wide-angle X-ray Scattering on a laboratory Xeuss 3.0 HR apparatus (Xenocs, Grenoble, France) equipped with a Dectris Ltd (Switzerland) 1 M Eiger2R movable detector and a Genix3D (Cu) X-ray source. A q-range from 0.01 to 1.9 $Å^{-1}$ was covered by measuring two sample-to-detector distances i.e. 0.06 and 0.9 m with an acquisition time of 900 and 1800 s respectively, calibrating the sample to detector distance by using silver behenate (lamellar scattering pattern with d = 58.376 Å). The scattering vector q is defined as $q = 4\pi/\lambda sin\theta$, where 2θ represents the scattering angle. All samples and pure water were measured in sealed borosilicate glass capillaries of internal diameter of 1.5 mm and under vacuum using a Peltier-controlled stage. To investigate the thermal behavior and the structural arrangement of the lipid core above the solid lipid melting point, SAXS measurements with temperature ramps were performed on the empty SLNs and NLCs samples. Firstly, the samples were measured at 20 °C, then at 70 °C (melting range 50–60 °C) and finally back at 20 °C to check the reversibility of the eventual structural modification following phase transition of the core. The 2D SAXS/WAXS patterns were radially averaged to obtain 1D patterns. Data reduction, normalization, background (water) subtraction and merging were performed by using XSACT (X-ray Scattering Analysis Calculation Tool) software (Xenocs, France). Fitting was performed with the SASView 6.0 software. The SAXS plots of SLNs were fitted using a combined core shell sphere (Tetyczka et al., 2019) multiplied to a broad peak model with the Plugin Add/Multiply function (SASView Documentation) (SasView documentation, xxxx), to account for the presence of organized lipid core domains and a poloxamer shell (Shah et al., 2016) as follows in Eqs. (3) and (4):

$$P(q) = \frac{scale}{V} F^2(q) + background \tag{3}$$

$$F(q) = \left[V_C(\rho_c - \rho_s) \frac{sin(qr_c) - qr_c cos(qr_c)}{(qr_c)^3} + V_s(\rho_s - \rho_{solv}) \frac{sin(qr_s) - qr_s cos(qr_s)}{(qr_s)^3} \right] \tag{4}$$

where V_s and V_C are the volumes of the sphere and core respectively, r_s and r_C are the radii of the particle and the core respectively, and ρ_c, ρ_s and ρ_{solv} are the scattering length densities of core, shell and solvent respectively. The broad peak model accounts for the presence of a broad peak representative of the scattering inhomogeneities of the core, as in Eq. (5):

$$I(q) = \frac{A}{q^n} + \frac{C}{1 + (|q - q_0|\xi)^m}^p + B \tag{5}$$

where q_0 is the peak position, A is the Porod law scale factor, n is the Porod exponent, C is the Lorentzian scale factor, m is the q exponent, ξ is the screening length and B the flat background.

For NLCs, a core shell bicelle model was used multiplied to a broad peak (Eq. (3)), where the form factor of a circular cylinder with a core shell scattering length density profile is described as follows in Eqs. (6) and (7):

$$I(Q,\alpha) = \frac{scale}{V_t} F(Q,\alpha)^2 \cdot sin(\alpha) + background \tag{6}$$

in which:

$$F(Q,\alpha) = \left[(\rho_c - \rho_f) V_C \frac{2J_1(QRsin\alpha)}{Q(R+t_r)sin\alpha} \frac{sin(QLcos\alpha/2)}{Q(L/2)cos\alpha} + (\rho_f - \rho_r) V_{c+f} \frac{2J_1(QRsin\alpha)}{QRsin\alpha} \frac{sin(Q(L/2+t_f)cos\alpha)}{Q(L/2+t_f)cos\alpha} + (\rho_r - \rho_s) V_t \frac{2J_1(Q(R+t_r)sin\alpha)}{Q(R+t_r)sin\alpha} \frac{sin(Q(L/2+t_f)cos\alpha)}{Q(L/2+t_f)cos\alpha} \right] \tag{7}$$

where V_t, V_c, and $V_c + f$ are the total volume of the bicelle, the volume of the core and volume of the core plus faces respectively, R is the core radius, L the core length, t_f and t_r the thicknesses of the face and rim respectively, and J is the first order Bessel function.

2.9. Synchrotron Small Angle X-ray Scattering measurements

Automated SAXS measurements of both empty and loaded systems with Resveratrol and Hydroquinone were performed at the high-brilliance BioSAXS P12 beamline operated by EMBL Hamburg at the PETRA III storage ring (DESY, Hamburg, Germany) (Blanchet et al., 2015). This undulator beamline was specifically designed for background-free detection of weakly-scattering macromolecular solutions and soft matter dispersion. The data were collected in automated batch mode, which allows in-vacuum continuous flow-through measurements and multi-frame data collection with an automated sampler (Round et al., 2015) (EMBL/ESRF). Full automation grants a high turnover rate and short sample exposure, thus minimizing radiation damage and with minimal volume consumption. A hybrid photon-counting pixel Pilatus 6 M detector (Dectris Ltd, Switzerland) was employed, with the wavelength of the incoming beam at 0.124 nm (10 keV) and a sample-to-detector distance of 3.1 m, covering a q-range of 0.02–4.5 nm^{-1}. The recorded 2D patterns were automatically collected, reduced, and processed thanks to the synchronized procedure developed on P12 (Franke et al., 2012).

2.10. Synchrotron time-resolved SAXS study of the assembly kinetics

The investigation of the assembly kinetics of empty SLNs and NLCs was performed at the high-brilliance Time-Resolved Small Angle X-ray Scattering ID02 beamline of the Extremely Brilliant Source (EBS) at the European Synchrotron Radiation Facility (ESRF, Grenoble, France) (Narayanan et al., 2022; Angelov et al., 2015). TR-SAXS is an advanced technique to probe assembly kinetics and transient structures on the tens up to hundreds of millisecond timescale. The coupling with a stopped-flow rapid-mixing device allows to mix and measure aqueous and organic phases at various volume ratios and flow rates with short dead times. The stopped-flow device is crucial in ensuring reproducibility of the experiments to obtain adequate statistics; moreover, the accuracy in measuring the early-stage processes and time evolution is granted by repetition of the same mixing sequences with appropriate delays. The high beam coherence and collimation with high reciprocal space resolution, together with sub-millisecond temporal resolution grant unparalleled possibilities to probe structure and dynamics of non-equilibrium soft matter nanosystems (Narayanan et al., 2014). The time-resolved 2D SAXS patterns were recorded using a high-sensitivity hybrid pixel-array Eiger2 4 M (Dectris AG) detector. The X-ray wavelength was 0.1 nm (12 keV) and the two chosen sample-to-detector distances were 1.5 m and 10 m, covering a total q-range from 0.0067 to 7.5 nm^{-1}. The online data reduction pipeline implemented on ID02 allows automatic masking, azimuthal regrouping and averaging of normalized 2D patterns to obtain the 1D profiles. The data acquisition sequence was hardware-triggered by a stopped-flow device SFM 4000 (BioLogic, Claix, France) with four stepper motor driven syringes and three mixers. A home-made flow-through capillary cell (diameter ~1.3 mm) is adapted to the mixing chamber and connected to the outlet of the last mixer. The aqueous and organic solutions were loaded in the device reservoirs and then mixed in the cell. The mixing protocol consisted of equal ratios of lipid solution in ethanol and surfactant solution in water, with a total flow rate of 4 mL/s and dead time of mixing of about 2 ms. Two different kinds of measurements were performed. Firstly, the onset of the assembly as a function of temperature was studied. This was fundamental since the mixing should happen in molten state, but the assembly kinetics of the solid lipid can only start below the molten-to-solid transition temperature. Both the stopped-flow reservoirs and cell were kept at 70 °C above the lipid melting point, then mixing and acquisitions in the cell were triggered while the cell was cooled to 25 °C at a rate of 1.5 °C/min. A scan of 100 frames was performed with 5 ms exposure per frame and 10 s of waiting time in between frames (about 3 frames recorded per minute, 1 frame every ≈0.5 °C). This allowed to identify the temperature at which the assembly starts.

Then, the second experiment consisted of a Time-resolved measurement where the cell temperature was fixed at 25 °C, while the solutions in the reservoirs were kept at 70 °C. Upon mixing, solidification of the lipidic core was induced by the lower temperature in the cell, and the kinetics of assembly induced by cooling of the mixed solutions was investigated. Scattering patterns were acquired following a geometric timestep series, with 5 ms of exposure time, 25 ms of initial deadtime d_0, 5 ms of delay *dead* multiplied by a factor of 1.22, acquiring 47 total frames. The deadtime [n] between the (n-1)th and nth frame was given by Eq. (8):

$$deadtime[n] = d_0 + dead \times factor^{n-1} \tag{8}$$

The total experiment time was given by the Eq. (9), and it was 261 s.

$$t = d_0 + \sum_0^{n-1}(dead \times factor^{n-1}) + exptime(n-1) \tag{9}$$

where t is the total time of the experiment, d_0 represents the initial dead time, *exptime* is the exposure and n is the number of acquired images.

3. Results and discussions

3.1. Dynamic light scattering and encapsulation efficiency

DLS and HPLC measurements performed on the entire set of synthesized samples (i.e. 192) are reported in full in the Supporting Information (Tables S1–S4). The measured responses, i.e. hydrodynamic diameter (or size), polydispersity index (PDI), and Encapsulation Efficiency (EE%) varied in the chosen design spaces as reported in Table 3 (here shown the minimum and maximum values obtained for each response). From the table below, it can be noted how the measured values for each response can vary in the design space, thus evidencing the need for rational optimization methods.

3.2. Experimental design

The measured responses in each proposed DoE were statistically analyzed, and either perturbation plots or response surfaces for all the studied systems are reported in Figs. S1–S12. These results model the variation of the experimentally studied responses (i.e. Size, PDI and Encapsulation efficiency) in all the described design spaces as a linear combination of the independent factors. The detailed discussion on the study of the experimental space of Resveratrol-loaded SLNs and NLCs, and Hydroquinone-loaded SLNs and NLCs respectively, is reported below. For each response, a statistical model was obtained, described by a linear equation (coded terms reported in Tables 1 and 2). In the equations, a plus (+) sign describes a synergistic effect (i.e. direct proportionality) of the factor to the measured response, whereas a minus (−) sign describes an antagonistic effect (i.e. indirect proportionality).

3.3. Study of the experimental space for resveratrol-loaded SLNs

DoE allowed to model the size of Resv-SLN (Table S5) as a linear combination of independent factors, after performing a reciprocal transformation of the raw dataset. The ANOVA indicated that the only factor that showed statistical influence on the size of Resv-SLN samples was C-FFR (Table S5, with determination coefficient $R^2 = 0.86$ reporting an adequate precision i.e. statistical signal-to-noise ratio of 16.34). The size model is then reduced to (Eq. (10)):

$$\frac{1}{size + 1} = 0.0104 + 0.0047C \tag{10}$$

where the factor C-FFR influenced synergistically the inverse of the size, meaning that using a higher aqueous-to-organic fractionated flow ratio results in smaller dimensions of the nanoaggregates. This was consistent with the role of the surfactant in stabilizing the nanosystem and pre-

venting aggregation. The significance of C in the model highlighted that the ratio of surfactant to lipids plays a relatively greater role in determining size than the individual concentrations of reagents, which were found to be non-significant factors to the size model.

The model of PDI ($R^2 = 0.70$, adeq. precision = 12.05) showed that only factors A-lipid concentration and C-FFR (Table S6) have statistical influence, since the inclusion of other factors significantly decreases the model fitting, meaning that they do not contribute to the model. Thus, variations in lipid concentration and lipid/surfactant ratio have a direct proportionality on PDI of Resv-SLN, as described by Eq. (11):

$$PDI = 0.233 + 0.028A + 0.051C \quad (11)$$

The analysis of encapsulation efficiency ($R^2 = 0.68$, adeq. precision = 11.82) showed that only two factors significantly contribute to the model, i.e. B-surfactant concentration and C-FFR (Table S7) that determined the encapsulation efficiency of resveratrol in SLNs following the linear relationship (Eq. (12)):

$$EE = +32.95 + 2.13B - 6.21C \quad (12)$$

The intercept of the curve (+32.95) denotes an overall high encapsulation efficiency for the nanosystems with an overall mean of 32.95 ±8.2 %. The antagonistic effect (minus sign in Eq.) of the FFR is mainly due to the increasing water fraction in the mixture and subsequent decrease of drug loading, as resveratrol is dissolved in the organic phase during the synthetical procedure.

3.4. Study of the experimental space for resveratrol-loaded NLCs

DoE allowed to model the size of Resv-NLC as a two-factor interaction, as all of the independent factors and their linear combinations had statistical influence on size. Indeed, F-values and p-values for all the included factors were significant (Table S8, $R^2 = 0.83$, adeq. precision 18.04). The linear combinations of factors A-lipid conc., B-surfactant conc., D-liquid lipid with factor C-FFR respectively, were included in the model even if not significant (p-value > 0.05), as their elimination does not improve the model itself. Indeed, the lack of statistical significance for the combination of total reagent quantity with the fractionated flow ratio (C) explains how a variation in one single factor has statistically more influence on size than both quantity and FFR. The size model is described by Eq. (13) where the negative coefficient of the two-factor interactions showed their antagonistic relationship to the size.

$$Size = 66.40 + 5.83A - 3.963B - 9.28C - 5.12D - 2.36AB - 1.87AC - 4.60AD - 1.23BC + 3.69BC - 0.12CD - 2.26ABC \quad (13)$$

To model the PDI an inverse square root transformation was applied to the raw dataset (Eq. (13)). Only factors A-lipid conc., B-surfactant conc., and C-FFR showed significant influence (Table S9) on the Polydispersity Index ($R^2 = 0.65$, adeq. precision 16.93). The synergistic influence of lipid concentration, and the antagonistic one of surfactant and FFR on the inverse square root of PDI is predicted by Eq. (14).

$$\frac{1}{\sqrt{PDI}} = 2.00 + 0.09A - 0.10B - 0.10C \quad (14)$$

The inclusion of independent factors A, B, and C in the linear model indicates that the PDI is influenced by the balance of FFR and of individual quantities of lipids and surfactants.

The model for encapsulation efficiency ($R^2 = 0.23$) indicated that no factor had statistical significance on EE% (Table S10). However, across the experimental runs, EE% ranged from 6.6 % to 42 %, with a mean value of 30.5±9.3 %. This was determined relative to a drug loading of 25 % or 33 %, depending on the FFR applied, thus for all the synthesized samples the EE% was in an appropriate range.

3.5. Study of the experimental space for hydroquinone-loaded SLNs

The full factorial design allowed to model the linear relationship between the factors and the power of the size of Hq-SLN, as in Eq. (15).

$$y' = y^{-1.28} \quad (15)$$

The ANOVA showed the statistical influence to the size of factors C-FFR and B-Surfactant concentration (Table S11, with $R^2 = 0.81$ and adeq. precision of 14.36). The synergistic effect of factor C denoted how increasing the FFR generally reduced the size of nanoaggregates, whereas the increase of surfactant concentration increased the size (Eq. (16)).

$$Size^{-1.28} = 0.003 - 0.0005B + 0.0014C \quad (16)$$

The model of the polydispersity index of Hq-SLN ($R^2 = 0.69$, adeq. precision 9.68) showed that all three independent factors had a statistical influence, including the linear combination AB (Table S12). The coded equation for the prediction of PDI (Eq. (17)) showed that the proportional change of both factors A-lipid concentration and B- surfactant concentration had a synergistic effect on the PDI, whereas the variation of one parameter while the other was kept constant lead to an antagonistic effect on the PDI.

$$PDI = 0.228 - 0.017A - 0.016B + 0.047C + 0.019AB \quad (17)$$

The model for Encapsulation Efficiency of Hq-SLN did not show any significant parameter and thus, the average value of all runs represented a better predicting parameter than the combination of different independent factors (average EE through 32 model runs: 11.5±1.8 %).

3.6. Study of the experimental space for hydroquinone-loaded NLCs

The full factorial design allowed to model the linear relationship between the factors and the power of the size of Hq-NLC, as described in Eq. (18):

$$y' = y^{-1.3} \quad (18)$$

All of the independent factors and some of their combinations had statistical influence in determining the size of Hq-NLC, according to a two-factor interaction model (Table S13, $R^2 = 0.84$, adeq. precision 15.87). The linear combinations of A-lipid conc., B-surfactant conc., D-liquid lipid respectively, with factor C-FFR were included in the model even if not significant (p-value >0.05), as their elimination did not improve the model itself. Moreover, as in the case of Resv-NLC the lack of statistical significance of the combination of total reagent concentration and the fractionated flow ratio (C) explains how a variation in one reagent had statistically more influence on size than the variation in both quantity and FFR. The model is then described by Eq. (19), where B-surfactant and A-solid lipid concentration showed an antagonistic effect on the size, whereas the linear combination of factors AB, AC, and AD presented a synergistic effect.

$$Size^{-1.3} = +0.003 - 0.0001A - 0.0003B + 0.012C + 0.0003AB + 0.0001AC + 0.0004AD \quad (19)$$

The linear relationship between factors and polydispersity index was modeled and the analysis showed that also third order interaction had statistical influence. The combination of factors A-lipid conc., C-FFR and D-liquid lipid showed a significant contribution to the PDI variation (p-value = 0.0058), resulting in a fit including all the second order interactions ($R^2 = 0.75$) (Table S14). Eq. (20) describes the linear variation of PDI as a function of the independent factors:

$$PDI = +0.2673 - 0.0217A + 0.0108B + 0.0389C + 0.0083D - 0.0146AC + 0.0073AD + 0.0161BD - 0.0046CD + 0.0214ACD \quad (20)$$

To model the encapsulation efficiency, the raw dataset has been

transformed as a power of 2.56, as in Eq. (21).

$$y' = y^{2.56} \tag{21}$$

In this case, ANOVA showed that factors with statistical influence were B-surfactant, C-FFR, D-liquid lipid and their linear combinations (BC, BD, CD) ($R^2 = 0.67$, adeq. precision 12.81). Independent variables with p-value > 0.05 (Table S15) were included to respect the hierarchy of the model. The exclusion of factor A-Lipid concentration was in accordance with the non-significance of the Encapsulation Efficiency model of Hq-SLN. On the contrary, the insertion of the liquid lipid fraction into the nanosystem was crucial in determining the encapsulation of hydrophilic molecules, by creating different structural domains and altering the order of the lipid core. Eq. (22) showed the synergistic effects of C-FFR in combination with liquid lipid (D) and surfactant concentration (B) respectively, whereas the combination of terms B and D had a negative effect on the vector's encapsulation efficiency.

$$EE^{2.56} = +528.02 + 17.38B - 21.25C - 29.60D + 70.72BC - 122.63BD + 133.37CD \tag{22}$$

Overall, both SLNs and NLCs systems appeared less suitable for the encapsulation of hydrophilic molecules, as the average encapsulation efficiency for the model hydrophilic molecule (Hydroquinone) is 11±1 % for Hq-SLN and 11±3 % for Hq-NLC, compared to Resveratrol, that is 32.9±8.2 % for Resv-SLN and 30.5±9.3 % for Resv-NLC. This is consistent with the composition of the solid lipid core, showing higher affinity with the hydrophobic model molecule that is more efficiently solubilized in the lipid core.

3.7. Nanosystems optimization

For each experimental design, the optimized formulation was obtained by using a desirability function with the aim of maximizing the encapsulation efficiency and minimizing the size and the PDI. This was done by assigning a major relative importance to increasing the encapsulation efficiency, as it represented the most challenging property to optimize. The optimal formulation for each system was prepared, and the models were validated. The experimental results, as well as optimized independent factors for each DoE (in coded terms) are reported in Table 4. Unloaded carriers were synthesized with the same optimized parameters, without adding Resveratrol or Hydroquinone respectively.

3.8. Differential scanning calorimetry

DSC analysis was performed to study the thermal properties, the crystallinity of the synthesized SLNs and NLCs and their suitability for dermal applications. Optimized loaded and unloaded samples were compared, and the bulk lipid was considered as a reference.

Table 4
Optimized experimental procedures for all samples, with independent factors expressed as coded values, predicted responses and experimentally measured responses with their standard deviations.

		Resv-SLN	Resv-NLC	Hq-SLN	Hq-NLC
A - Lipid Concentration (mg/mL)		−1	+1	+1	+1
B - Surfactant Concentration (mg/mL)		+1	−1	−1	−1
C - FFR		−0.15	+1	0.42	+1
D - Liquid Lipid (%)		–	+1	–	+1
Size (nm)	**Predicted**	99	45	70	65
	Experimental	108.0 ±2.5	55.4±1.8	75.4±2.4	60.1±0.1
PDI	**Predicted**	0.2	0.19	0.18	0.23
	Experimental	0.19 ±0.04	0.23 ±0.02	0.22 ±0.04	0.26 ±0.04
EE (%)	**Predicted**	34	40	12	14
	Experimental	36.0±4.7	37.2±3.8	11.5±1.8	12.4±1.1

The melting peak shown in the empty nanosystems thermograms was broader, less intense and had a lower onset temperature with respect to the bulk Precirol (Fig. 1a). This could be attributed to the nanometric particle size, high specific surface area and the presence of surfactant (Zimmermann et al., 2005; Teeranachaideekul et al., 2008). In addition, in the melting event of SLNs two peaks were detectable (Fig. 1b) in contrast to the bulk lipid thermogram which showed only a single peak at 54.28 °C. According to the literature, the peak at lower temperature shown in the SLNs thermogram (50.27 °C) can be attributed to the metastable α form of Precirol and the higher one (53.16 °C) to the stable β form (Teeranachaideekul et al., 2007). For NLCs instead, the melting event presented lower melting point, enthalpy and calculated crystallization index with respect to the SLNs, which was given by the formation of a less ordered crystalline matrix due to the incorporation of Oleic acid (Severino et al., 2012) (Fig. 1a). Indeed, NLCs and SLNs have both nanometric sizes, meaning that the difference in the melting point cannot be due to differences in particle size. Additionally, the difference between the maximum and the onset temperature increased in the order bulk lipid < SLNs < NLCs, further indicating an increased disorder of the lipid liquid-crystalline core and generation of an amorphous structure (Sakellari et al., 2021) (Fig. 1a). The incorporation of the two cargo molecules into the nanocarriers did not alter critically the solid lipid melting point both in SLNs and NLCs (Fig. 1b and c), indicating that the lipid remained in the same polymorphic form. However, the crystallization index slightly increased upon hydroquinone incorporation and slightly decreased upon resveratrol incorporation in SLNs; on the contrary, it decreased in both Resv-NLC and Hq-NLC, suggesting that the drugs interacted differently with the lipid molecular packing in each system.

The onset melting temperatures of SLNs and NLCs were in the range of 48 °C and 35 °C respectively, making these nanoparticles suitable for dermal applications, as they are compatible with the human skin temperature of around 32 °C. The higher percentage of crystallinity in SLNs was consistent with the presence of higher organization in the solid core with respect to NLCs (Table 5).

3.9. Laboratory Small Angle X-ray Scattering measurements

Preliminary structural characterization was performed on a lab SAXS instrument to assess the inner organization of unloaded SLNs and NLCs samples, firstly in the equilibrium state at 20 °C and then above the melting transition temperature (70 °C) of the solid lipid. The 1D intensity plots of SLNs at 20 °C showed a broad bump centered at q = 0.13 $Å^{-1}$ (d = 48.4 Å) indicative of the presence of organized domains in the solid core that was seen as well in the NLCs plot, at q values of 0.127 $Å^{-1}$ (Fig. 2). In the latter case, an additional bump was evidenced at q = 0.047 $Å^{-1}$ (d = 134 Å), indicative of additional supramolecular organization given by the liquid lipid (Fig. 2). This would suggest a broader organization of the lipidic core in the NLCs sample, i.e. less tightly packed domains of the solid lipid. Here, the first bump corresponded to the repetition of solid domains, and the second bump was likely given by both solid and liquid lipids structured together, where the Oleic acid shell intercalated in the defects of Precirol ATO 5 domains. WAXS measurements performed on both samples showed a small peak at q = 1.4 $Å^{-1}$ corresponding to d = 4.48 Å (Fig. 2, enlargement), that is the typical spacing of triglyceride intermolecular aggregation (Corkery et al., 2007; Wa Kasongo et al., 2011).

By increasing the temperature above the melting transition temperature of the Precirol ATO 5, the SLNs sample showed complete destructuring and loss of organization of the core as expected, which was then fully restored upon cooling back to 20 °C (Fig. 3, left). On the other hand, NLCs sample showed a different thermal behavior and slightly less reversibility of the solid core structure. The curve recorded at 70 °C showed that the broad peak of the solid lipid organization became broader and shifted at higher q = 0.26 $Å^{-1}$, evidencing less ordered domains at smaller length scales, whereas the intercalated liquid lipid

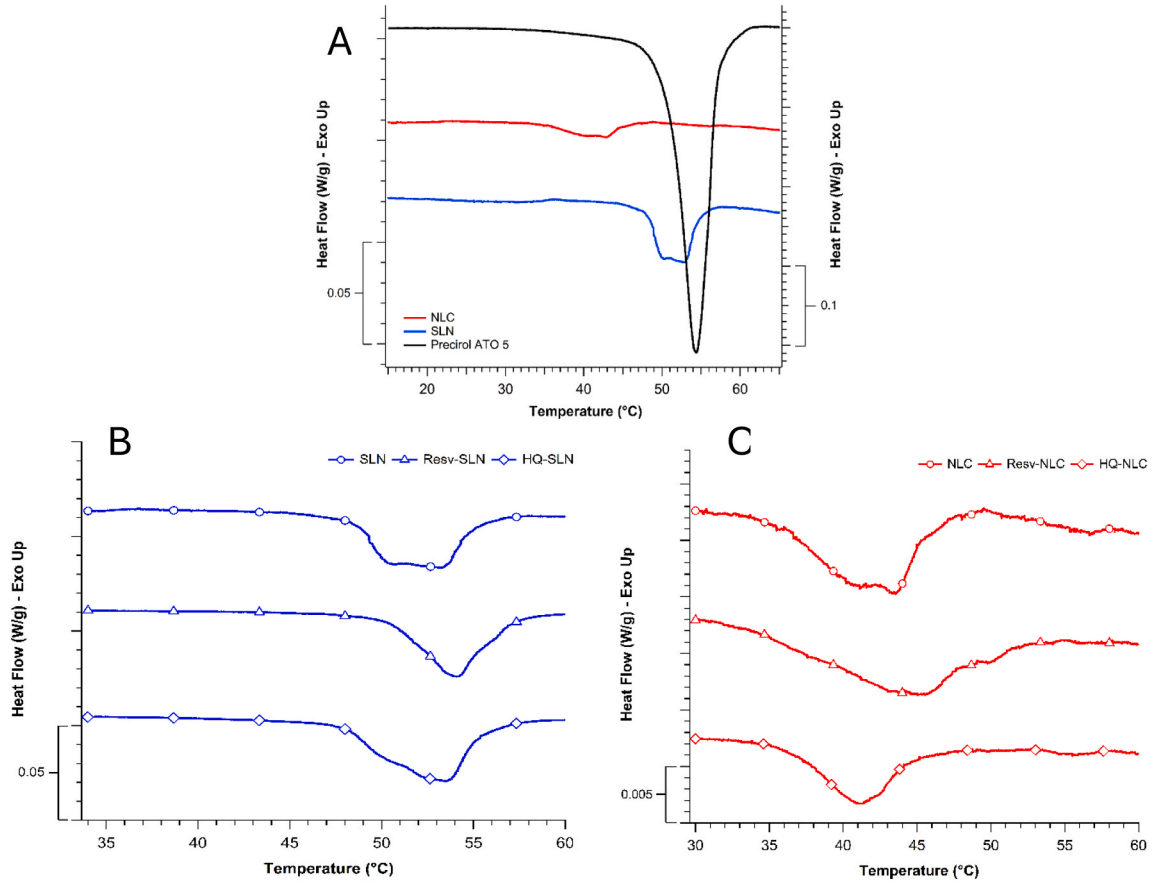

Fig. 1. (a) DSC thermograms of Precirol ATO 5 (black), unloaded SLNs (blue) and unloaded NLCs (red). The scale on the left axis is referred to SLNs and NLCs, while the one on the right refers to Precirol ATO 5. (b) comparison between unloaded SLNs, Resv-SLN, and Hq-SLN, (c) comparison between unloaded NLCs, Resv-NLC, and Hq-NLC.

Table 5
Thermal data and crystallization index (χ%) of empty SLNs, NLCs, loaded nanocarriers and bulk lipid samples.

	Bulk precirol ATO 5	SLN	Resv-SLN	Hq-SLN	NLC	Resv-NLC	Hq-NLC
T onset (°C)	50.77	48.62	50.64	47.85	35.05	34.38	36.51
T max (°C)	54.38	53.16	54.08	53.48	43.56	45.06	41.07
Enthalpy (J/g)	118.80	4.64	4.05	4.92	1.63	1.46	0.88
χ%	–	78.11	68.18	82.83	54.88	49.16	29.62

domains remained unchanged (Fig. 3, right). Thus, the solid core appeared to be more amorphous due to the temperature increase but still partially structured, likely due to the intercalating Oleic acid that maintained some degree of organization. By cooling back to 20 °C, the Precirol ATO 5 peak became more resolved and shifted back to slightly lower q values, however the original spacing and shape was only partially restored. This evidenced the different structural response and rearrangement capability of SLNs and NLCs to thermal phenomena, where the liquid lipid induced a higher structural flexibility. This property could result in higher cargo stability and slower release over time typical of NLCs (Samaridou et al., 2020). The increased disorder in the lipidic core organization of the NLCs was consistent with the DSC analysis, where a 13 °C decrease in the solid lipid melting point was observed and a lower crystallinity percentage was found.

For SLNs, a sphere core radius of 23.5 Å and a shell thickness of 11.8 Å were obtained, whereas for NLCs a bicelle core radius of 11 Å and a thickness of rim and face of 85 Å and 237 Å was found (Tables S16 and S17); here, the rim and face both consisted of the Poloxamer shell acting both as a coating and capping of the cylindrical bicelle (Kanwar et al., 2019).

In parallel, DLS measurements in temperature were performed to investigate the changing in the overall dimension of unloaded SLNs and NLCs during melting of Precirol ATO 5 (Figs. S13 and S14). For SLNs, the autocorrelation function shifted to shorter times with increasing temperature, indicating a slight decrease in hydrodynamic radius probably due to the sol-gel transition of the Poloxamer shell, reported in the 40–50 °C range. A similar trend was observed for NLCs; however, the shift in the autocorrelation function was less pronounced, which could suggest the partial interaction of the hydrophobic moieties of Poloxamer with liquid lipid domains (Shaikhullina et al., 2020). For both systems, the particle size returned to its initial value upon cooling back to 25 °C.

3.10. Static synchrotron Small Angle X-ray measurements

The static synchrotron SAXS data collected at room temperature of both empty and loaded SLNs and NLCs samples confirmed the preliminary evidence obtained with lab SAXS on empty samples (Fig. 2). Indeed, the broad bumps in unloaded SLNs and NLCs were found at the q positions already identified, whereas some variations could be noticed for Hydroquinone and Resveratrol loaded ones (Fig. 4). Specifically, 1D curves of SLNs samples showed the same position of the broad bump in all the nanocarriers. This evidenced that cargo loading did not influence the spacing of the solid core, it only made it slightly more ordered, as

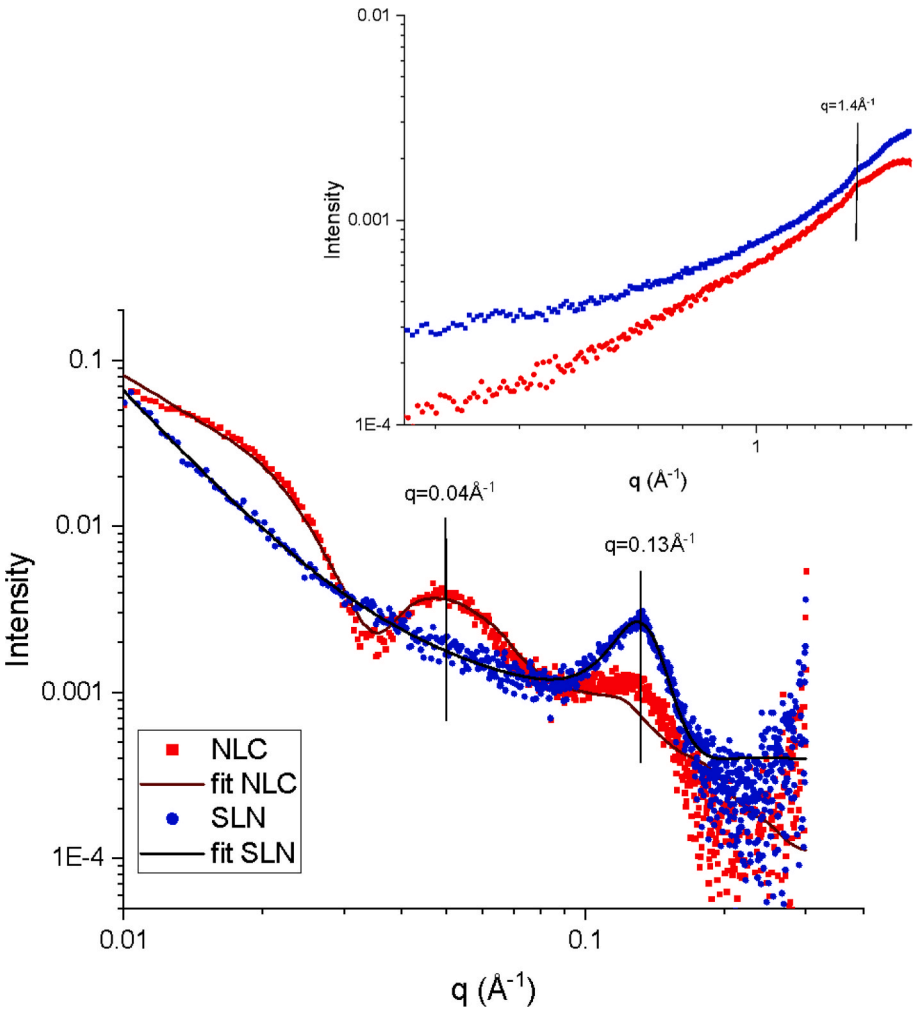

Fig. 2. Static SAXS and WAXS (enlargement) measurements of unloaded SLNs and NLCs with fitting curves superimposed.

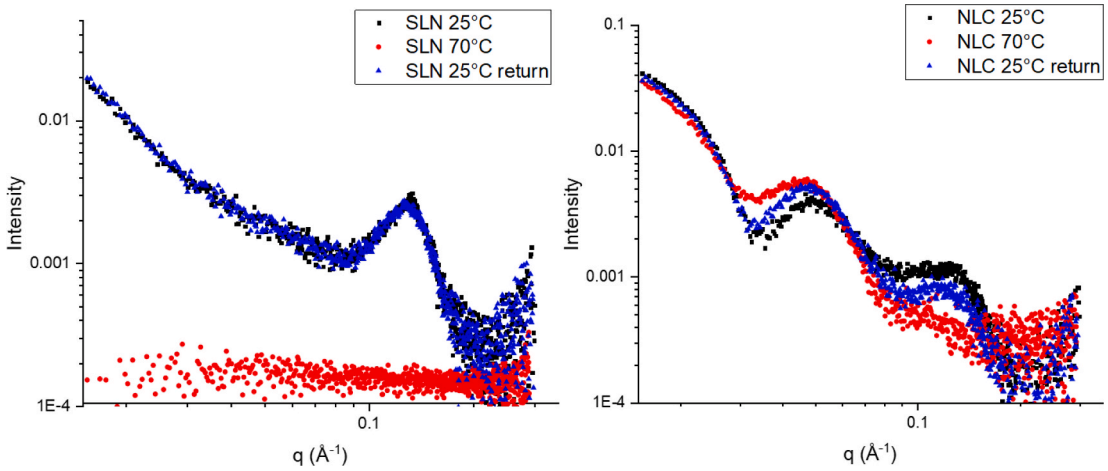

Fig. 3. Static SAXS measurements of SLNs (left) and NLCs (right) at 25 °C (black), 70 °C (red) and returning back to 25 °C (blue).

shown by the presence of sharper bumps in Hq-SLN and Resv-SLN. Regarding the slope of the curves at intermediate q, empty SLNs showed a q^{-2} slope indicative of a prevalence of flat disk shape, whereas Hq-SLN and Resv-SLN showed a q^{-3} slope, evidencing prevalence of a globular shape. Thus, it could be hypothesized that compound encapsulation induced a small transition to adjust to cargo loading. This was also confirmed by the slight modification in the form factor parameters to adjust to the presence of the intercalated drugs (Table S18). In the case of NLCs samples, the two bumps found in the empty nanovector at $q = 0.13$ Å^{-1} and $q = 0.048$ Å^{-1} were found to be modified by the presence of encapsulated molecules. Indeed, the bump showing the packing of the solid core was less defined, whereas the second bump reflecting the presence of solid/liquid lipids domains was shifted at lower q values (0.033 Å^{-1}). This indicated the presence of larger, loosely

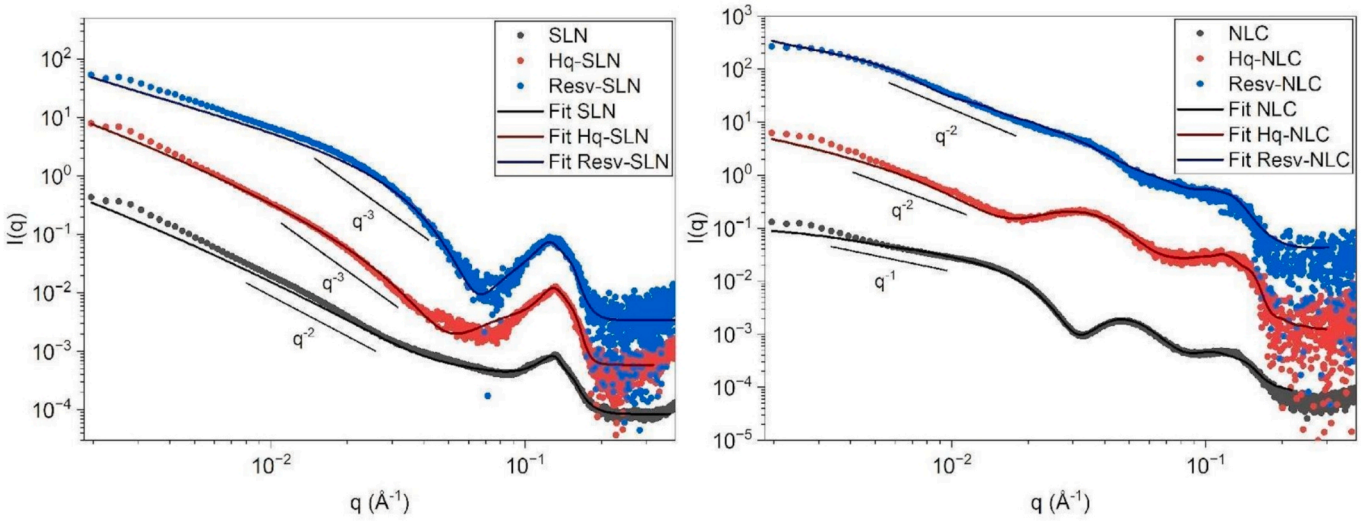

Fig. 4. Synchrotron Static SAXS measurements of optimized SLNs and NLCs samples with superimposed fitting curves.

packed assemblies due to drug (Table S19) solubilization in the liquid domains. Here, the slope of the intensity plots was q^{-1} for unloaded NLCs, indicating a cylinder shape and q^{-2} for loaded samples, showing a flat disk shape. Thus, the nature of encapsulated cargo did not dramatically modify the structuring of SLN core, its presence only induced formation of more ordered domains, particularly in the case of the hydrophobic compound. This confirms the rigid core structure in SLNs. On the contrary, in NLC samples the nature of the loaded cargo

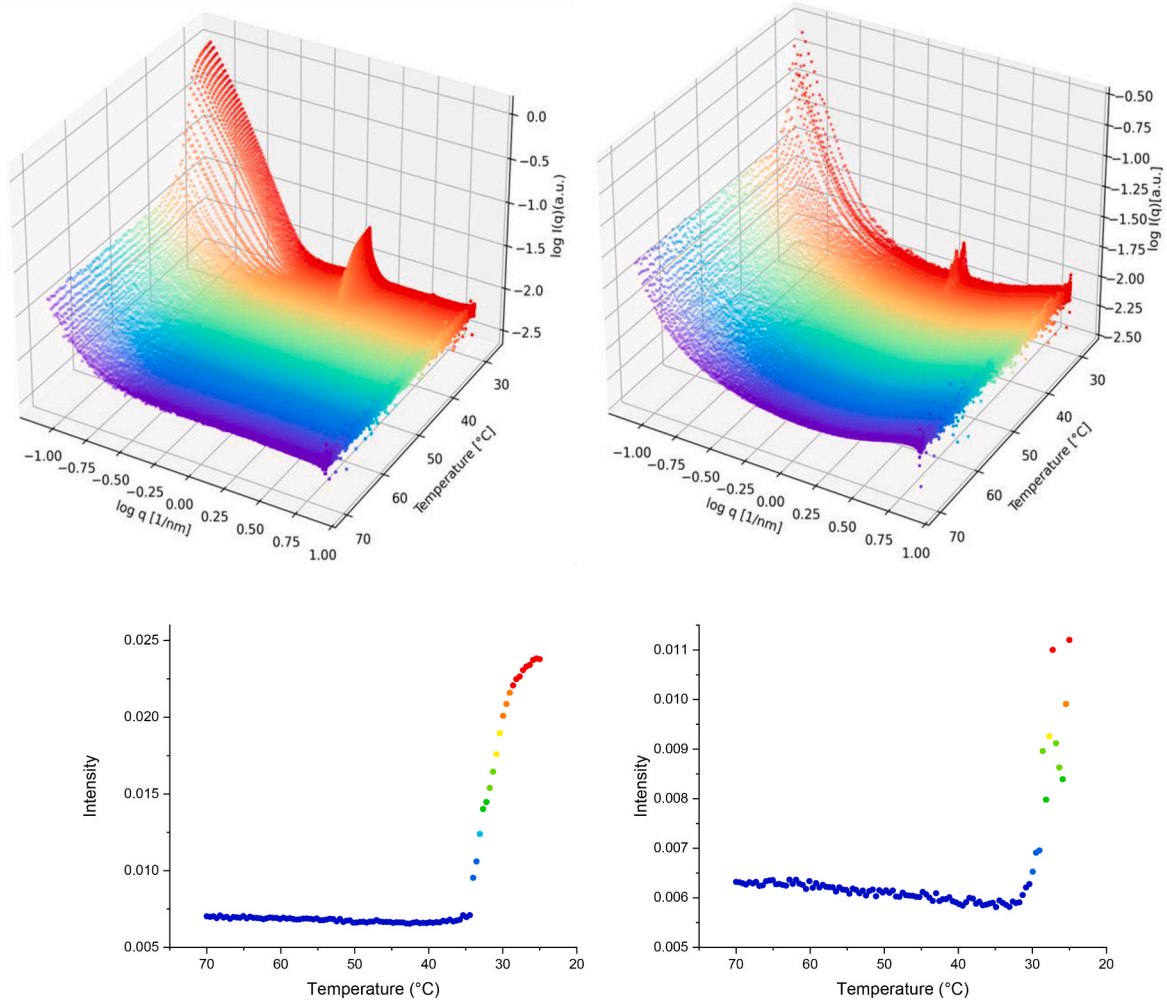

Fig. 5. Top row: SLNs (left) and NLCs (right) SAXS intensity plots (in log I(q)vs log q scale) recorded taking one frame every 0.5 °C, cooling down from 70 to 28 degrees to identify the starting temperature point of aggregation. Bottom row: Peak intensity at fixed q (1.27 nm^{-1}) plotted against temperature.

showed significant impact on the curves, particularly on the liquid lipid arrangement. A de-structuring effect was given mainly by the hydrophobic cargo molecule, while the hydrophilic cargo only shifted the bump assigned to solid-liquid domains at lower q values, resulting in an increase of the domains size.

3.11. Synchrotron time-resolved Small Angle X-ray scattering (Tr-SAXS) measurements

SAXS experiments with a stopped-flow rapid-mixing setup were performed to investigate the kinetics of assembly of SLNs and NLCs induced by contextual phase mixing and cooling. This experiment was meant to simulate as closely as possible the conditions of microfluidic mixing and assembly of these samples. Firstly, several static SAXS temperature scans were performed after triggering the mixing with the stopped-flow. Indeed, the mixing of the aqueous and organic phases should occur at 70 °C, above the solid–liquid transition of the Precirol ATO 5, but the assembly is later triggered by cooling down below the molten-to-solid transition. Thus, this allowed us to precisely identify the temperature onset of assembly evidenced by the start of peak formation at 37 °C for SLNs and 32 °C for NLCs, respectively (Fig. 5). This was consistent with the presence of Oleic acid in the NLCs core, lowering the phase transition temperature of the system as already observed with DSC analyses (Table 3). Indeed, the presence of the liquid component intercalating and interacting with Precirol ATO 5 altered the regular packing of the solid core, resulting in a less ordered and more fluidly packed phase at lower temperatures compared to the pure lipid core. The higher order and organization of the solid core in SLNs was evidenced by the presence of an intense first order peak and a smaller second order one, whereas in NLCs only one peak with lower intensity was shown. These experiments were conducted on empty nanocarriers only, since the evidence found by Differential Scanning Calorimetry showed only slight differences in the thermal properties of loaded nanocarriers with respect to unloaded ones. On the contrary, large differences were found according to nanocarrier type (SLNs or NLCs) due to the major influence on the assembly start temperature given by the lipid components. In Fig. 5 (lower panel) the variation in intensity of the aggregation peak of the lipid core of both nanosystems is shown as a function of temperature.

Then, once the temperatures of assembly were identified, Tr-SAXS measurements with the stopped-flow device were performed at 25 °C (Figs. 6 and 7), that is a sufficiently low temperature for both samples to cool the mixed phases and start the assembly. This was crucial to investigate the kinetics of assembly of the nanocarriers triggered by phase mixing (Tenchov et al., 2021; Müller et al., 2002; Vandoolaeghe et al., 2009; Maeki et al., 2024). The stopped-flow syringes were kept at 70 °C, whereas the cell was kept at 25 °C. This temperature dependence resulted in a delay of the assembly kinetics of about 9 s for SLNs, needed for the mixture to start cooling down and reach 37 °C, i.e. that is where the peak of the ordered solid core appeared (Fig. 6). It is possible to see that full peak intensity was only reached after 20–25 s, where also a second small peak is evidenced at $q = 3.8\ nm^{-1}$ (light green curve). This data was consistent with static SAXS results, both from lab SAXS and synchrotron, showing a more defined broad peak centered at $q = 1.27\ nm^{-1}$. It is possible to evidence that the slope changed during the assembly, from a q^{-2} slope, indicative of a prevalence of flat disks in the first seconds, to a q^{-3} slope indicating globular shape when the equilibrium state was approached. This highlighted the formation of metastable aggregates during SLNs assembly kinetics, that were rapidly stabilized in the final form on the scale of hundreds of seconds.

In the case of NLCs sample (Fig. 7) the assembly with peak formation at 32 °C corresponded to 25 s delay, showing a smaller, less intense peak centered at $q = 1.26\ nm^{-1}$, and a q^{-3} slope of globular aggregates for the entire assembly. Interestingly, even though peak position recorded during time-resolved measurements was consistent with static curves, the broad bump at lower q identified in these latter was not shown and the slope was different. This suggested that, even though the assembly kinetics seemed to be completed at the end of the acquisition steps, i.e. almost 5 min after mixing was triggered, NLCs samples might undergo a slower arrangement in the following hours. Indeed, static measurements were performed 24 h after microfluidic preparation and storage of samples at 4 °C, whereas the fast kinetics probed by Tr-SAXS covered from milliseconds to minutes after nanocarrier formation. Contrarily to the solid core of SLNs, that appeared to stabilize quickly after formation in its equilibrium end state, for NLCs the presence of liquid and solid lipids in the core resulted in higher order right after formation, which then was stabilized in a less organized state at lower energy. It can be hypothesized that during the aggregation oleic acid was excluded by the Precirol ATO 5 domains, and it was more likely to interact with the hydrophobic moieties of Poloxamer, hence the sharper peak with respect to SLNs plots. However, this represented a transient aggregation state on a longer timescale with respect to SLNs. Indeed, in the final stable state oleic acid intercalated in the defects of the solid core, that slowly rearranged after several hours from the synthesis. Moreover, after the final state was reached, NLCs structure appeared to be more flexible and resistant to temperature shifts, as shown by lab SAXS in temperature (Fig. 3). This behavior was in stark contrast with SLNs, whose core stabilized quickly during formation and was disrupted by temperature increase.

4. Conclusions

In this work, we optimized the synthesis of microfluidic-fabricated Solid Lipid Nanoparticles and Nanostructured Lipid Carriers by exploring a design space defined by compositional and instrumental

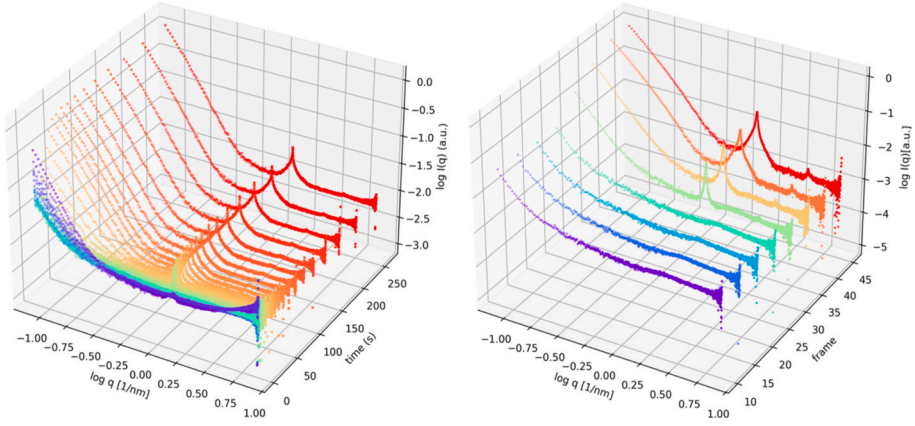

Fig. 6. Time Resolved SAXS of Solid Lipid Nanoparticles (in log I(q)vs log q scale). Left: complete timescale studied, right: average of 5 different measurements reported each 5 frames.

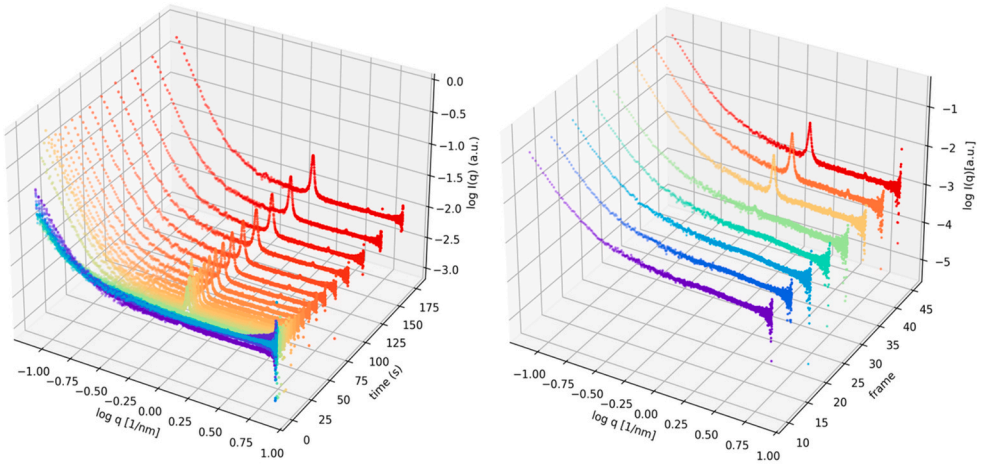

Fig. 7. Time Resolved SAXS of Nanostructured Lipid Carriers (in log I(q)vs log q scale). Left: complete timescale studied, right: average of 5 different measurements reported each 5 frames.

parameters, and statistically modeling three properties as responses i.e. size, PDI and encapsulation efficiency of two model drugs. The model was validated by synthesizing and characterizing the optimized nanocarriers. Subsequently the thermal behavior, the supramolecular structure at equilibrium and the kinetics of assembly on the millisecond timescale of the optimized formulations were thoroughly investigated. The experimental design allowed to statistically analyze the influence of the chosen parameters on nanocarriers size, monodispersity and capability to encapsulate resveratrol and hydroquinone. Particularly, for resveratrol-loaded SLNs the FFR was the main influencing factor on all three responses, as lower FFR resulted in larger size, smaller PDI and higher EE%, whereas lower lipid concentration and higher surfactant concurred only to these latter two. On the contrary, for NLCs the combination of compositional factors as lipid, surfactant and liquid lipid concentrations were more relevant on the size and PDI, whereas no parameter was significant for EE%. It should be emphasized that both SLNs and NLCs showed high EE% for resveratrol (considering also the high drug loading used), and the optimized systems showed sizes and PDI appropriate for delivery. In the case of hydroquinone-loaded SLNs, the relevance of FFR on size was again evidenced as for Resv-SLN, whereas for PDI the concentrations of lipid and surfactant also played a role. Finally, for hydroquinone-loaded NLCs the combination of compositional parameters was more relevant on size than the FFR, whereas for EE% surfactant, liquid lipid and FFR all concurred. Thus, for SLNs the instrumental parameter of the aqueous-to-organic phase ratio generally influences the outcomes more than for NLCs, where the combination of solid/liquid lipid and surfactant needs to be carefully adjusted. Moreover, both SLNs and NLCs have proven more efficient as carriers for hydrophobic compounds, as expected considering their composition and structure. These results highlighted the relevance of cargo affinity to carrier composition and evidenced how each parameter should be rationally balanced for each specific carrier and drug. The investigation of the thermal behavior performed by DSC showed a higher degree of crystallinity of SLNs with respect to NLCs, that is consistent with the presence of intercalated Oleic acid in the NLCs core. Moreover, the largest effect on the melting temperatures was given by lipid composition, whereas cargo loading did not substantially affect the thermal behavior. These data were in excellent agreement with lab and synchrotron SAXS measurements. These experiments showed complete melting of SLNs core, and rearrangement only of NLCs core in response to heating; moreover, core structuring occurred at different temperatures in the two nanocarriers. The solid lipid core organization was not substantially modified upon cargoes encapsulation, whereas the liquid lipid organization was influenced by solubilization of the hydrophobic cargo. These data showed that different carrier/cargo affinity partially influences core structure and interactions. Advanced Time-resolved SAXS measurements evidenced that the aggregation kinetics of both SLNs and NLCs is highly temperature- and composition dependent; indeed, a delay in the start of assembly up to several seconds, according to the temperature was shown. The presence of liquid lipid more than doubled this delay in NLCs with respect to SLNs, and it was responsible for crucially different kinetic behavior. Indeed, it should be emphasized that SLNs reached their final stable state after tens of seconds from the start of peak formation, maintaining the same structural arrangement after hours or days as shown by static SAXS. On the contrary, the kinetics of NLCs appeared to reach only a transient plateau in the aggregation during time-resolved measurements. Its equilibrium end state was only reached after several hours, showing rearrangement of the core as the liquid lipid intercalated the defects of the solid lipid lattice. Thus, SLNs showed fast aggregation and transition to the final form with lower stability to temperature increase, whereas NLCs aggregated slowly with a long transient state, and had higher stability when the final form was reached. This is in accordance with the widely accepted concept of NLCs as less structured aggregates with respect to SLNs, allowing slower core adjustments and longer stability. This finding could have relevant implications in the shelf life and leakage protection of the formulations.

In conclusion, microfluidic synthesis guided by Design of Experiments ensures the fabrication of formulations with optimal physicochemical properties to be employed as nanocarriers for drug delivery. In combination with this approach, the advanced thermal and structural characterization gives precious insights on the fundamental mechanisms of thermal response, assembly kinetics, structural organization and stability, that directly impact on the biofunctionality of nanocarriers. We believe that this fundamental knowledge, combined with the systematic design and synthetic approach could grant enhanced control, higher safety and efficacy, and contribute significantly to lipid nanoparticles research and transferability.

List of Chemical Compounds included in this work

Precirol ATO 5 (glyceryl palmitostearate).
Poloxamer 407 (Oxirane, methyl-, polymer with oxirane).
Oleic Acid (*cis*-9-octadecanoic acid).
Resveratrol (3,4′,5-*trans*-trihydroxystilbene).
Hydroquinone (benzene 1–4 diol).

CRediT authorship contribution statement

Giulia Gabbricci: Writing – original draft, Methodology, Investigation, Conceptualization. **Luigi Talarico:** Writing – original draft,

Investigation, Formal analysis, Conceptualization. **Ilaria Clemente:** Writing – original draft, Investigation, Formal analysis, Conceptualization. **Aleksi Sutinen:** Writing – review & editing, Investigation, Data curation. **Clément E. Blanchet:** Writing – review & editing, Investigation, Data curation. **Duccio Tatini:** Writing – review & editing, Validation, Investigation. **Gemma Leone:** Writing – review & editing, Validation, Data curation. **Agnese Magnani:** Supervision, Resources, Project administration, Funding acquisition.

Funding

This work is funded by the European Union—NextGenerationEU within the Italian Piano Nazionale di Ripresa e Resilienza, Missione 4 Componente 2, PNRR M4C2—Investimento 1.5. Creazione e rafforzamento di "ecosistemi dell'innovazione", costruzione di "leader territoriali R&S"—Progetto THE (Tuscan Health Ecosystem)—Spoke 4—Nanotechnologies for diagnosis and therapy. Project code ECS00000017, CUP B63C22000680 007.

Declaration of competing interest

The authors declare the following financial interests/personal relationships which may be considered as potential competing interests: Agnese Magnani reports financial support was provided by European Union. If there are other authors, they declare that they have no known competing financial interests or personal relationships that could have appeared to influence the work reported in this paper.

Acknowledgements

The static synchrotron SAXS data was collected at beamline P12 operated by EMBL Hamburg at the PETRA III storage ring (DESY, Hamburg, Germany). We acknowledge EMBL for beamtime allocation and the entire beamline staff for assistance in using the beamline.

The Tr-SAXS data were collected at the ID02 beamline of the European Synchrotron Radiation Facility (ESRF, Grenoble, France). We acknowledge the ESRF for provision of synchrotron radiation facilities under proposal number SC-5594 and we would like to thank Dr. Gouranga Manna for assistance and support in using beamline ID02. SAXS data will be publicly available after Sep 2027 at DOI: 10.15151/ESRF-ES-1830822950.

We thank CSGI (Florence, Italy) for DSC and lab SAXS beamtime, and particularly Prof. Emiliano Fratini and Dr. Gavino Bassu for technical support and assistance.

Appendix A. Supplementary data

Supplementary data to this article can be found online at https://doi.org/10.1016/j.ijpharm.2025.126441.

Complete experimental design tables and graphs, i.e. statistics and surface plots; Dynamic Light Scattering Intensity plots and correlograms in temperature from 25 to 70 °C; tables of fitting parameters for SAXS data; representative chromatograms.

Data availability

ESRF SAXS data are available as mentioned in the acknowledgements section.

References

Sebastiani, F., Yanez Arteta, M., Lerche, M., Porcar, L., Lang, C., Bragg, R.A., Elmore, C. S., Krishnamurthy, V.R., Russell, R.A., Darwish, T., Pichler, H., Waldie, S., Moulin, M., Haertlein, M., Forsyth, V.T., Lindfors, L., Cárdenas, M., 2021. Apolipoprotein E binding drives structural and compositional rearrangement of mRNA-containing lipid nanoparticles. ACS Nano 15 (4), 6709–6722. https://doi.org/10.1021/acsnano.0c10064.

Samaridou, E., Heyes, J., Lutwyche, P., 2020. Lipid nanoparticles for nucleic acid delivery: current perspectives. Adv. Drug Deliv. Rev. 154–155, 37–63. https://doi.org/10.1016/j.addr.2020.06.002.

Tenchov, R., Bird, R., Curtze, A.E., Zhou, Q., 2021. Lipid Nanoparticles—from liposomes to mRNA vaccine delivery, a landscape of research diversity and advancement. ACS Nano 15 (11), 16982–17015. https://doi.org/10.1021/acsnano.1c04996.

Müller, R.H., Radtke, M., Wissing, S.A., 2002. Solid Lipid Nanoparticles (SLN) and Nanostructured Lipid Carriers (NLC) in cosmetic and dermatological preparations. Adv. Drug Deliv. Rev. 54, S131–S155. https://doi.org/10.1016/S0169-409X(02)00118-7.

Campani, V., Giarra, S., De Rosa, G., 2018. Lipid-based core-shell nanoparticles: evolution and potentialities in drug delivery. OpenNano 3, 5–17. https://doi.org/10.1016/j.onano.2017.12.001.

Koroleva, M., Portnaya, I., Mischenko, E., Abutbul-Ionita, I., Kolik-Shmuel, L., Danino, D., 2022. Solid lipid nanoparticles and Nanoemulsions with solid shell: physical and thermal stability. J. Colloid Interface Sci. 610, 61–69. https://doi.org/10.1016/j.jcis.2021.12.010.

Sakellari, G.I., Zafeiri, I., Batchelor, H., Spyropoulos, F., 2021. Formulation design, production and characterisation of Solid Lipid Nanoparticles (SLN) and Nanostructured Lipid Carriers (NLC) for the encapsulation of a model hydrophobic active. Food Hydrocolloids for Health 1, 100024. https://doi.org/10.1016/j.fhfh.2021.100024.

Khater, D., Nsairat, H., Odeh, F., Saleh, M., Jaber, A., Alshaer, W., Al Bawab, A., Mubarak, M.S., 2021. Design, preparation, and characterization of effective dermal and transdermal lipid nanoparticles: a review. Cosmetics 8 (2), 39. https://doi.org/10.3390/cosmetics8020039.

Spinozzi, F., Moretti, P., Perinelli, D.R., Corucci, G., Piergiovanni, P., Amenitsch, H., Sancini, G.A., Franzese, G., Blasi, P., 2024. Small-angle X-ray scattering unveils the internal structure of lipid nanoparticles. J. Colloid Interface Sci. 662, 446–459. https://doi.org/10.1016/j.jcis.2024.02.076.

Wang, Y., Cai, R., Chen, C., 2019. The nano–bio interactions of nanomedicines: understanding the biochemical driving forces and redox reactions. Acc. Chem. Res. 52 (6), 1507–1518. https://doi.org/10.1021/acs.accounts.9b00126.

Chang, D.P., Jankunec, M., Barauskas, J., Tiberg, F., Nylander, T., 2012. Adsorption of lipid liquid crystalline nanoparticles: effects of particle composition, internal structure, and phase behavior. Langmuir 28 (29), 10688–10696. https://doi.org/10.1021/la301579g.

Chen, D., Love, K.T., Chen, Y., Eltoukhy, A.A., Kastrup, C., Sahay, G., Jeon, A., Dong, Y., Whitehead, K.A., Anderson, D.G., 2012. Rapid discovery of potent SiRNA-containing lipid nanoparticles enabled by controlled microfluidic formulation. J. Am. Chem. Soc. 134 (16), 6948–6951. https://doi.org/10.1021/ja301621z.

Arduino, I., Liu, Z., Rahikkala, A., Figueiredo, P., Correia, A., Cutrignelli, A., Denora, N., Santos, H.A., 2021. Preparation of Cetyl palmitate-based PEGylated solid lipid nanoparticles by microfluidic technique. Acta Biomater. 121, 566–578. https://doi.org/10.1016/j.actbio.2020.12.024.

Maeki, M., Uno, S., Niwa, A., Okada, Y., Tokeshi, M., 2022. Microfluidic technologies and devices for lipid nanoparticle-based RNA delivery. J. Control. Release 344, 80–96. https://doi.org/10.1016/j.jconrel.2022.02.017.

Gimondi, S., Ferreira, H., Reis, R.L., Neves, N.M., 2023. Microfluidic devices: a tool for nanoparticle synthesis and performance evaluation. ACS Nano 17 (15), 14205–14228. https://doi.org/10.1021/acsnano.3c01117.

Pepic, I., Hafner, A., Lovric, J., Perina Lakos, G., 2014. Nanotherapeutics in the EU: an overview on current state and future directions. Int. J. Nanomed. 1005. https://doi.org/10.2147/IJN.S55359.

Talarico, L., Pepi, S., Susino, S., Leone, G., Bonechi, C., Consumi, M., Clemente, I., Magnani, A., 2023. Design and optimization of solid lipid nanoparticles loaded with triamcinolone Acetonide. Molecules 28 (15), 5747. https://doi.org/10.3390/molecules28155747.

González-Fernández, F.M., Bianchera, A., Gasco, P., Nicoli, S., Pescina, S., 2021. Lipid-based nanocarriers for ophthalmic administration: towards experimental design implementation. Pharmaceutics 13 (4), 447. https://doi.org/10.3390/pharmaceutics13040447.

Shah, B., Khunt, D., Bhatt, H., Misra, M., Padh, H., 2015. Application of quality by design approach for intranasal delivery of Rivastigmine loaded solid lipid nanoparticles: effect on formulation and characterization parameters. Eur. J. Pharm. Sci. 78, 54–66. https://doi.org/10.1016/j.ejps.2015.07.002.

Tavares Luiz, M., Santos Rosa Viegas, J., Palma Abriata, J., Viegas, F., Testa Moura de Carvalho Vicentini, F., Lopes Badra Bentley, M.V., Chorilli, M., Maldonado Marchetti, J., Tapia-Blácido, D.R., 2021. Design of Experiments (DoE) to develop and to optimize nanoparticles as drug delivery systems. Eur. J. Pharmaceutics and Biopharmaceutics 165, 127–148. https://doi.org/10.1016/j.ejpb.2021.05.011.

Duong, V.A., Nguyen, T.T.L., Maeng, H.J., 2020. Preparation of solid lipid nanoparticles and nanostructured lipid carriers for drug delivery and the effects of preparation parameters of solvent injection method. Molecules 25 (20), 1–36. https://doi.org/10.3390/molecules25204781.

Tetyczka, C., Hodzic, A., Kriechbaum, M., Juraić, K., Spirk, C., Hartl, S., Pritz, E., Leitinger, G., Roblegg, E., 2019. Comprehensive characterization of nanostructured lipid carriers using laboratory and synchrotron X-ray scattering and diffraction. Eur. J. Pharm. Biopharm. 139, 153–160. https://doi.org/10.1016/j.ejpb.2019.03.017.

SasView documentation. www.sasview.org.

Shah, R.M., Bryant, G., Taylor, M., Eldridge, D.S., Palombo, E.A., Harding, I.H., 2016. Structure of solid lipid nanoparticles produced by a microwave-assisted microemulsion technique. RSC Adv. 6 (43), 36803–36810. https://doi.org/10.1039/C6RA02020H.

Blanchet, C.E., Spilotros, A., Schwemmer, F., Graewert, M.A., Kikhney, A., Jeffries, C.M., Franke, D., Mark, D., Zengerle, R., Cipriani, F., Fiedler, S., Roessle, M., Svergun, D.I.,

2015. Versatile sample environments and automation for biological solution X-ray scattering experiments at the P12 beamline (PETRA III, DESY). J. Appl. Cryst. 48 (2), 431–443. https://doi.org/10.1107/S160057671500254X.

Round, A., Felisaz, F., Fodinger, L., Gobbo, A., Huet, J., Villard, C., Blanchet, C.E., Pernot, P., McSweeney, S., Roessle, M., Svergun, D.I., Cipriani, F., 2015. BioSAXS sample changer: a robotic sample changer for rapid and reliable high-throughput X-ray solution scattering experiments. Acta Crystallogr. D Biol. Crystallogr. 71 (1), 67–75. https://doi.org/10.1107/S1399004714026959.

Franke, D., Kikhney, A.G., Svergun, D.I., 2012. Automated acquisition and analysis of small angle X-ray scattering data. Nucl. Instrum. Methods Phys Res A 689, 52–59. https://doi.org/10.1016/j.nima.2012.06.008.

Narayanan, T., Sztucki, M., Zinn, T., Kieffer, J., Homs-Puron, A., Gorini, J., Van Vaerenbergh, P., Boesecke, P., 2022. Performance of the time-resolved ultra-small-angle X-ray scattering beamline with the extremely brilliant source. J. Appl. Cryst. 55 (1), 98–111. https://doi.org/10.1107/S1600576721012693.

Angelov, B., Angelova, A., Drechsler, M., Lesieur, S., 2015. Rapid Mixing Stopped-Flow Small-Angle X-Ray Scattering Study of Lipoplex Formation at Beamline ID02@ESRF. J. Surf. Investigation. X-ray, Synchrotron and Neutron Techniques 9 (1), 105–110. https://doi.org/10.1134/S1027451015010279.

Narayanan, T.; Gummel, J.; Gradzielski, M. Probing the Self-Assembly of Unilamellar Vesicles Using Time-Resolved SAXS; 2014; pp 171–196. Doi: 10.1016/B978-0-12-418698-9.00007-1.

Zimmermann, E., Souto, E.B., Müller, R.H., 2005. Physicochemical investigations on the structure of drug-free and drug-loaded Solid Lipid Nanoparticles (SLN^{TM}) by means of DSC and 1H NMR. Pharmazie 60 (7), 508–513.

Teeranachaideekul, V., Boonme, P., Souto, E.B., Müller, R.H., Junyaprasert, V.B., 2008. Influence of oil content on physicochemical properties and skin distribution of Nile red-loaded NLC. J. Control. Release 128 (2), 134–141. https://doi.org/10.1016/j.jconrel.2008.02.011.

Teeranachaideekul, V., Souto, E.B., Junyaprasert, V.B., Müller, R.H., 2007. Cetyl palmitate-based NLC for topical delivery of coenzyme Q10 – development, physicochemical characterization and in vitro release studies. Eur. J. Pharm. Biopharm. 67 (1), 141–148. https://doi.org/10.1016/j.ejpb.2007.01.015.

Severino, P., Pinho, S.C., Souto, E.B., Santana, M.H.A., 2012. Crystallinity of Dynasan®114 and Dynasan®118 matrices for the production of stable Miglyol®-loaded nanoparticles. J. Therm. Anal. Calorim. 108 (1), 101–108. https://doi.org/10.1007/s10973-011-1613-7.

Corkery, R.W., Rousseau, D., Smith, P., Pink, D.A., Hanna, C.B., 2007. A case for discotic liquid crystals in molten triglycerides. Langmuir 23 (13), 7241–7246. https://doi.org/10.1021/la0634140.

Wa Kasongo, K., Shegokar, R., Müller, R.H., Walker, R.B., 2011. Formulation development and in vitro evaluation of didanosine-loaded nanostructured lipid carriers for the potential treatment of AIDS dementia complex. Drug Dev. Ind. Pharm. 37 (4), 396–407. https://doi.org/10.3109/03639045.2010.516264.

Kanwar, R., Gradzielski, M., Prevost, S., Kaur, G., Clemens, D., Appavou, M.-S., Mehta, S. K., 2019. Effect of lipid chain length on nanostructured lipid carriers: comprehensive structural evaluation by scattering techniques. J. Colloid Interface Sci. 534, 95–104. https://doi.org/10.1016/j.jcis.2018.08.066.

Shaikhullina, M., Khaliullina, A., Gimatdinov, R., Butakov, A., Chernov, V., Filippov, A., 2020. NMR relaxation and self-diffusion in aqueous micellar gels of Pluronic F-127. J. Mol. Liq. 306, 112898. https://doi.org/10.1016/j.molliq.2020.112898.

Vandoolaeghe, P., Barauskas, J., Johnsson, M., Tiberg, F., Nylander, T., 2009. Interaction between Lamellar (Vesicles) and nonlamellar lipid liquid-crystalline nanoparticles as studied by time-resolved small-angle X-ray diffraction. Langmuir 25 (7), 3999–4008. https://doi.org/10.1021/la802768q.

Maeki, M., Kimura, N., Okada, Y., Shimizu, K., Shibata, K., Miyazaki, Y., Ishida, A., Yonezawa, K., Shimizu, N., Shinoda, W., Tokeshi, M., 2024. Understanding the effects of ethanol on the liposome bilayer structure using microfluidic-based time-resolved small-angle X-ray scattering and molecular dynamics simulations. Nanoscale Adv. 6 (8), 2166–2176. https://doi.org/10.1039/D3NA01073B.